CVPR
#1292

CVPR 2008 Submission 1292. CONFIDENTIAL REVIEW COPY. DO NOT DISTRIBUTE.

CVPR
#1292

Fluid Motion Estimation Method based on Physical Properties of Waves

H. Sakaino

NTT Energy and Environment Systems Lab.

s.hidetomo@lab.ntt.co.jp

Abstract

This paper presents a fluid flow estimation method for ocean/river waves, clouds, and smoke based on the physical properties of waves. Most of the previous optical flow methods based on fluid dynamics/mechanics estimate a smooth flow using a continuity equation and/or div-curl velocity constraint. However, abrupt or inhomogeneous image motion changes in such fluid-like images are not estimated well. In this paper, we assume that many fluid-like motion changes are due to wave phenomena that lead to a brightness change. Thus, a wave generation equation is applied with a two-step optimization. A novel constraint based on the velocity-frequency relationship equation and a wave statistical property are used. The results of experiments on synthetic and real image sequences show the validity of our method.

1. Introduction

Methods of detecting the apparent motion of fluid-like motion in a video of, for example, clouds, ocean/river waves, and smoke have been one of the intensive research topics in computer vision [1-10]. A number of optical flow models based on fluid dynamics have been reported [1-5, 7], where a continuity equation is used to follow a certain property of the fluid [2-4], and a smoothness velocity constraint is used based on the first derivative of a velocity [3, 11] or the divergence-curl (div-curl) equation [2, 7]. However, the previous methods fail to achieve local detection of an abrupt motion change in a fluid image sequence. Almost all complicated motion and shape changes in a fluid-like image come from at least two factors: first, natural phenomena can change dynamically in an irregular manner, and second, a flow can move in multiple directions rather than a single direction. For example, the activities of clouds [2], smoke [22], and ocean waves [19] can be caused by complicated wind changes which play an essential role in changing image brightness. The resulting images show inhomogeneous texture over time ranging from smooth and discontinuous motion. Thus, we assume that these fluid-based phenomena are governed by a wind-induced waves' physical property. In ocean engineering [18, 19], irregular and multidirectional properties of a wave have been extensively simulated. Because of the wave model, both the smoothness and discontinuity in image brightness are likely to be correlated with the change in a wave. In this paper, we present a wave phenomenon-based optical flow framework for a fluid-like image. A wave generation equation from ocean engineering [19] is used to model an image brightness change intergrated with the [10]'s basic model. To constrain the estimated velocity, a velocity-frequency relation equation [14, 15, 19] and a statistical property of the wave phenomenon [18, 19] are applied. Optical flow and wave related parameters are obtained by a two-step optimization algorithm using two consecutive images. In experiments, using synthetic and real image sequences, it is shown that our model surpasses a previous simple sinusoidal wave equation model [8] and two previous fluid-based optical flow models [2, 3]. The smooth and discontinuous motion in the inhomogeneous image brightness of clouds, for example, as estimated by our method is estimated visually plausible, whereas the previous methods estimate only smooth and uniform motion, thus validating the effectiveness of our method for fluid-like images.

2. Related work

In recent years, a number of methods of estimating an optical flow from a fluid-like image sequence [1] have been widely reported. A fluid-like image such as cloud can change its shape and brightness over time in a much more complicated way than a rigid or elastic object. Thus, most of the previous methods utilize the fluid dynamics model. Corpetti et al. [2] applied a continuity equation [3] to estimate a satellite image of clouds with a div-curl velocity constraint. The continuity equation in fluid dynamics stands for the mass conservation law in a region and this equation links the density and velocity of a fluid parcel. The volumic mass is identified as an image intensity. Nakajima et al. [4] used the Navier-Stokes (NS) equation and a continuity equation as a velocity constraint. These previous methods are based on an image brightness constancy assumption. Zhou et al. [5] approximated the velocity of cloud motion by using an Affine motion model. They applied it to an infrared image to recover the height of the cloud using the NS and continuity equation. For an infrared cloud image, Bereziat et al. [6] modeled a total image brightness invariance of an object. This model is needed to segment object regions where the total brightness invariance principle is applicable. Otsuka et al. [20] used a spatiotemporal image for a nearly uniform flow with at least 15 frames and their nonphysical method [20] can not detect a locally abrupt image intensity change in fluid-like

CVPR
#1292

CVPR 2008 Submission 1292. CONFIDENTIAL REVIEW COPY. DO NOT DISTRIBUTE.

CVPR
#1292

images, i.e., rotation. Arnaud et al. [7] improved the accuracy of optical flow estimation using a Schlieren image sequence. However, this method is likely to be effective only in the specific image experiment system. A water surface [18] and image sequence over time show development and decay with a shape and brightness change in a much shorter period than in a cloud image sequence as explained above. Thus, river and ocean wave image sequences are very challenging objects for stable estimation of dense optical flow. Using a harmonic oscillation equation, Sun et al. [16] estimated one component of ocean wave motion in a video indirectly from a unidirectionally swaying yacht in a harbor with a manual setting. Thus, flow waves with various orientations were ignored. Holland [14] and Spencer et al. [15] analyzed many basic wave properties, such as the wave frequency and wavelength from a wave video of a seashore/the ocean in sunlight. In their methods, a dispersion relationship, which we also use, played a central role in deriving wave-related physical parameters. This relationship is a function of velocity and frequency but they did not detect optical flow from a video. In an experimental room, Jahne et al. [13] estimated the orientation of wave motion and their methods were high effective at utilizing image intensity to estimate wave activity. Murase [8] used a simple sinusoidal wave equation with pattern matching to estimate a regular wave change in a wave. However, an object on the tank bottom can be viewed from the water surface. Thus, his model was very specific to an indoor regular wave. Doretto et al. [22] synthesized a temporal/dynamic texture based on the ARMA model using number of image. However, the model learns a periodical change without optical flow. In computer graphics, a great number of wave animation methods have been presented using a wave generation model [17]. However, many wave-related parameters such as frequency must be manually defined with random numbers. No optical flow models from a wave video have been used.

3. Wave Phenomenon Model

3.1. Wave physical properties of fluid-like image

  As mentioned above, in optical flow modeling, previous fluid-dynamics-based equations and velocity constraints are obviously insufficient to represent all necessary properties such as wave physical properties in a fluid-like image, i.e., a discontinuity. Thus, we will discuss a wave generation model as shown in Figure 1. Three examples of fluid-like phenomena, hurricane (cloud) [2], smoke [22], and wave are shown (a). Cross-section profiles between two dotted lines corresponding to image intensity in each of the three real images are shown in (b). The respective image intensity changes over time at three points selected

from between the dotted lines of (a) are shown in (c). The characteristics of the three phenomena are as follows: First, a satellite radar cloud/infrared image changes over time with the development and decay process, which is caused by a convective wind flow. Thus, the local brightness in an image response to a rotating flow in both vertical and horizontal directions. Second, in rising and diffusing smoke, blowing wind plays a central role in organizing a wavy pattern. On the surface of smoke [22], the image brightness changes over time due to an inhomogeneous wind flow. Third, in an ocean/river image, apparently, the water surface, for example, shows an elevated displacement, which creates a trough and crest over time. This phenomenon is activated by wind [19]. As a result, the shape and texture of a water surface can change over time. As mentioned above, most of the fluid-like phenomena in an image are likely to show a locally wavy change as well as a change in brightness. In order to model this, we refer to a wave generation theory (model) [18, 19] and in this paper, we extend this model to make it suitable for estimating the optical flow of cloud and smoke as well as water waves.
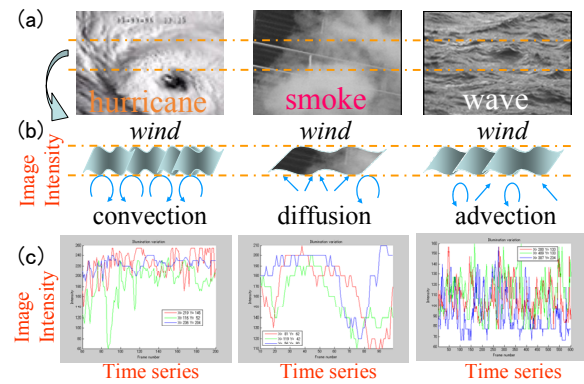

Figure 1: Wave-like activities of fluid-like images: (a) Images of three fluid-like phenomena: hurricane, smoke, and waves. (b) Illustration of wave patterns created by wind. (c) Intensity change in a wave-like image at three points in the respective three images.

3.2. Basic wave equation

  From a linear wave generation theory [19], a multi-directionality irregularity (MI) model is known. Regular motion means a periodical change while irregular motion means nonstationarity. The MI model is represented as shown in (1). In this paper, $H(x, y, t)$ represents the image intensity (brightness) at pixel coordinates (x, y), at time t.

$$H(x,y,t) = \sum_{m=1}^{M} a_m^* \cos(k_m^{x*} x \cos\theta_m^* + k_m^{y*} y \sin\theta_m^* - 2\pi f_m^* t + \varepsilon_m), \quad (1)$$

where a_m^*, $(k_m^{x}, k_m^{y})^*$, f_m^*, θ_m^*, and ε_m are amplitude, wavenumber components, frequency, orientation, and noise, respectively. The performance of this equation has been verified by many wave experiments. This equation

CVPR #1292

CVPR 2008 Submission 1292. CONFIDENTIAL REVIEW COPY. DO NOT DISTRIBUTE.

CVPR #1292

includes two important properties: first, a wave moves not in a single direction but in almost all directions. A principle (strongest) wave flow exists along with subordinate weak flows. Second, it has a wide spectrum of frequency, amplitude, wavenumber, wavelength, height, and orientation. As a result, a wave shows an irregular height change as shown in Figures 2 in the examples in two dimensions (a) and one dimension (b). Here, (a) was simulated using (1), which combines a number of cosine functions up to M (~150). The wave-like image intensity change in Figure 1(c) shows a visually similar trend to the plot in Figure 2(b). Based on the characteristics of (1), we assume that the wave activity in an image sequence follows the MI model. Thus, since the image brightness change is modeled as (1), the accuracy of optical flow estimation will be enhanced.
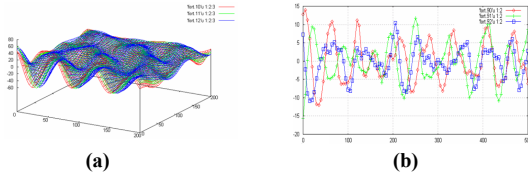

(a)   **(b)**

Figure 2: Example of a simulated irregular wave profile: (a) Two-dimensional waves using (1). (b) Time series versus the height of one-dimensional three plots at three points in (a).

3.3. Modified wave generation model

Normally, when (1) is used, the order of M must be empirically set to over 100 to randomly approximate a wave frequency up to a higher frequency term. However, this is too large for our purpose. To reduce this order, we use one of the physical properties of waves [19]. It is known that the more the frequency and height a wave increases, the smaller the wavenumber becomes. Thus, we aim to treat a higher frequency property by a smaller order M term as follows. Based on the above property, the simplest modification to (1) is to multiply the amplitude by $1/m$ and the wavenumber, frequency, and orientation by m as shown in (2), where m is an integer and $m > 0$. For example, when the orientation θ becomes $m\theta$, both the cosine and the sine functions have a higher frequency. For our parameter estimation purpose, the noise term can be ignored.

$$H(x,y,t) = \sum_{m=1}^{M} a_m \cos(x k_m^x \cos\theta_m + y k_m^y \sin\theta_m - 2\pi f_m t). \quad (2)$$

where $\quad a_m \leftarrow a_m^* / m, \; k_m^x \leftarrow k_m^{x*} \cdot m, k_m^y \leftarrow k_m^{y*} \cdot m, \; f_m \leftarrow f_m^* \cdot m,$
and $\theta_m \leftarrow \theta_m^* \cdot m.$

3.4. Optical flow model

In a video, we assume that image brightness changes over time according to (2). In order to integrate (2) into the optical flow framework, we apply the model of Haussecker et al. [10]. As shown in (3), an image brightness variation

model can be described. On the left, ∇, $\mathbf{w}$, and I are the first spatial derivative, velocity (optical flow), and image intensity (brightness), respectively and I_t is the first temporal derivative. If the right side is zero, this shows the image brightness constancy. Otherwise, the image brightness will change according to the physical phenomenon of wave. Haussecker et al. [10] used such as a heat diffusion model with no velocity constraint. In this paper, we apply (2) to the term on the right side of (3). As a result, (2) is transformed into (4), in which the optical flow components, $\mathbf{w} = (u, v) =$ $(dx/dt, dy/dt)$. Pyramidal image processing when the size of an image over 20 x 20 pixels is used to cope with a large displacement in a video.

$$\nabla I \cdot \mathbf{w} + I_t = \frac{d(physics)}{dt}, \quad (3)$$

where $\nabla \equiv \partial/\partial x + \partial/\partial y$, $I_x^n \equiv (I_{i+1,j}^n - I_{i,j}^n)/\Delta x$, $I_y^n \equiv (I_{i,j+1}^n - I_{i,j}^n)/\Delta y$
$I_t \equiv (I_{i,j}^{n+1} - I_{i,j}^n)/\Delta t$, $\Delta x = \Delta y = 1.0$.

$$\frac{d(physics)}{dt} = \frac{d(H(x,y,t))}{dt}. \quad (4)$$

3.5. Velocity constraint

When we are solving (3) and (4), a velocity constraint will enhance the estimation accuracy and stability. We use two velocity constraints: a smoothness constraint and a (modified) dispersion relationship constraint. The first one is used because of the nature of fluidity and the second one is a novel constraint in computer vision. From a wave theory [19], the relationship between the wavenumber and angular frequency [15, 19] is defined as shown in (5).

$$\omega^2 = gk \tanh(kh), \quad (5)$$

where $\omega = 2\pi f$, k, h, and g are angular frequency, wave number, water depth, and gravity acceleration, respectively. The other basic variables are the period, $T = 1/f$, wavelength, $L = 2\pi/k$, and velocity, $c = |\mathbf{w}| = (u^2 + v^2)^{1/2}$, where $c = L/T = \omega/k$. From (5), we obtain a new velocity constraint as shown in (6): (*For details, see appendix A*).

$$c^2 \propto |\gamma - f^2|^{1/2}, \text{ where } \gamma = \frac{3g}{16\pi^2 h}. \quad (6)$$

3.6. Objective function

We define the objective function E (7) to estimate two optical flow components along with five wave-related parameters which are the two wavenumber components, frequency, amplitude, and orientation. α was set to 0.001.

$$E(u, v, k_m^x, k_m^y, f_m, a_m, \theta_m) = \sum_{\Omega \in R2} \rho_{\text{img\_var}}(e_0, \sigma) +$$
$$\lambda_1 \sum_{\Omega \in R2} \rho_{\text{wave\_constraint}}(e_1, \sigma) + \lambda_2 \sum_{\Omega \in R2} \rho_{\text{smooth\_constraint}}(e_2, \sigma), (7)$$

CVPR
#1292

CVPR 2008 Submission 1292. CONFIDENTIAL REVIEW COPY. DO NOT DISTRIBUTE.

CVPR
#1292

where $\rho(z,\sigma) = \log\left(1+0.5(z/\sigma)^2\right)$, $\partial\rho/\partial e = 2e/(2\sigma^2+e^2)$,

$e_0 = \left|It+Ixu+Iyv-\dfrac{\partial H}{\partial t}\right|$, $e_1 = |u^2+v^2-\alpha^2(\gamma-f_m^2)^{1/2}|$, $e_2 = |u_x^2+u_y^2+v_x^2+v_y^2|$.

On the right hand side of (7), the first term represents the variation in image brightness in an MI model (2). The second and third terms show the wave constraint of (6) and smoothness constraint imposed by the first spatial derivative, respectively. (7) can be solved by a least-squares method. To avoid the influence of outliers [12] in an image, we apply the Lorentzian robust function ρ. Two consecutive images are input and computed in a two-dimensional region $\Omega \in R^2$. To minimize (7), the Conjugate Gradient method is applied, where numerical differencing is used to obtain the first derivative of E (7) with respect to seven variables.
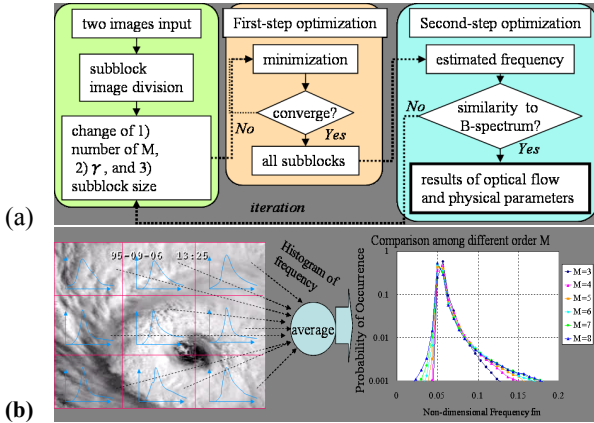

(a)

(b)

Figure 3: Algorithm for estimating optical flow and wave-related parameters using the physical properties of wave. (a) Overview of a two-step optimization for estimation. (b) Second step of the optimization based on a histogram of frequency in each subblock and an averaged frequency profile.

3.7. Two-step optimization

When minimizing (7), we must define three parameters of an order M, γ, and the subblock size of an image, $\Omega \in R^2$ in advance. Figure 3(a) shows our algorithm for estimating optical flow and wave-related parameters in a two-step optimization. An image is divided into several subblocks (b), the size of which is related to the motion speed per frame. The order M (2) is related to the range of high frequency bandwidth. The γ influences the magnitude of a discontinuity in motion. The first optimization is locally performed in each subblock where three parameters of a subblock size, an order M, and γ are provided with respective initial values. Since the optimal combination of these three parameters is estimated locally, consistency of flow is needed among neighboring subblocks. Thus, we introduce a global optimization as the second optimization

estimating three parameters such as M. For this, we rely on a theoretical property of wave [19]. We utilize the Bredtschneider energy spectrum equation (8).

$$B(f) = 0.257H_{1/3}^2T_{1/3}(T_{1/3}f)^{-5}\exp\{-1.03(T_{1/3}f)^{-4}\}. \quad (8)$$

Here, $H_{1/3}$ and $T_{1/3}$ are defined as *the significant wave height* and *the significant frequency*, respectively. This profile has one peak as shown in Figure 10(a), where the horizontal and vertical axes show a non-dimensional frequency and energy spectrum, respectively. This unique profile was obtained experimentally when wind blew over a water surface. Since it has a non-dimensional frequency and Figure 1(c) shows a wave-like change caused by the wind, we assume that this profile holds true for smoke and hurricane image sequences as well. To obtain the relationship between a non-dimensional frequency and energy, as shown in Figure 3(b), we assume that the number of pixel in frequency is proportional to the magnitude of the energy spectrum. Multiple profiles shown in (b) can be obtained ranging over six orders, M = 3~8 when γ and the subblock size are fixed. In order to choose one profile from six, we can find the closest profile to the Bredtschneider profile (8) when we obtain the minimum error for using (9). In (9), a function of an $Est(f)$ is computed by summing the histograms of all subblocks in an image when M and γ are fixed. The other unknown parameters of subblock size and γ are also interchanged as in (a). Thus, all unknown parameters are optimized through the two-step optimization process. Note that a subblock in an image is shifted per pixel.

$$(M,\gamma,subblock)_{opt} = \underset{M,\gamma,subblock}{arg\ min}|\textstyle\sum_f B(f)-Est(f)_{M,\gamma,subblock}|. \quad (9)$$

4. Experiment on Synthetic Images

To show the validity of our model, we conducted several experiments all of which used two consecutive images. For a fluid-like real image sequence, it is difficult to quantize estimated data. Therefore, we first synthesized a test image sequence with ground truth flow data. In this simulation, we wanted to create a wavy image sequence. To do this, we use two fluid-dynamics-based numerical models : the advection (AD) equation and the Navier- Stokes (NS) equation [21]. The AD equation can update an image intensity over time along with a given velocity vector field and the NS equation can update a velocity vector field. Therefore, what we need is to provide a complicated velocity field using [21]. Thus, a wavy fluid-like synthesized image sequence can be simulated. Using one real wave image at time t (Fig. 4(a)), we generated a deformed image at time $t+1$ (b). The original image was borrowed from Figure 8 (b). In Figure 4, a complicated velocity field with two large vortexes, one

CVPR
#1292

CVPR 2008 Submission 1292. CONFIDENTIAL REVIEW COPY. DO NOT DISTRIBUTE.

CVPR
#1292

counterclockwise and the other clockwise wise, and wavy flows (c) were defined and the AD equation was then applied with (a) and (c) to generate (b). The flow sketch in (d) clarifies what flow was used. Note that many discontinuous flow changes around each vortex have been defined. The ground truth of the velocity field was compared with the flow fields estimated by our method and by three previous methods [2], [3], and [8] (*details given in Appendix B*). [2] is based on a div-curl velocity constraint (DC model), and [3] is also based on a continuity equation model (WS model) with a smooth velocity constraint. A simple sinusoidal wave equation from [8] was also used (SIN model) in place of the MI based equation (2).
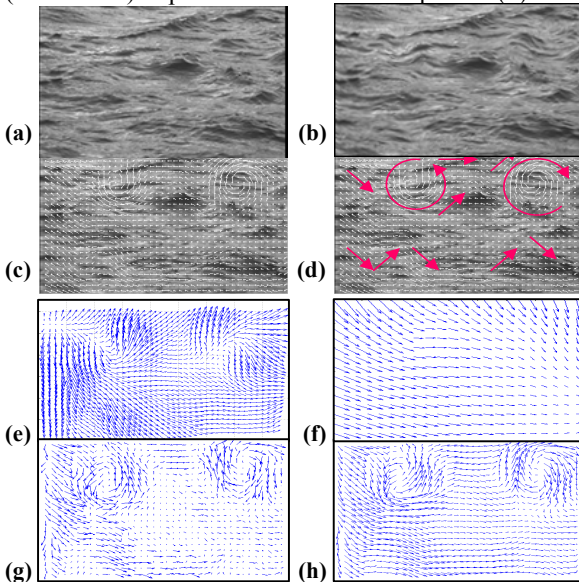

Figure 4: Synthesitc test image sequence at time t (a) and, at time t+1 (b). (c) The given flow. (d) Flow sketch. (e) DC model. (f) WS model. (g) SIN model. (h) Our MI model.
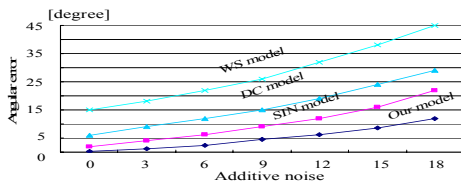

Figure 5: Comparison of three methods for synthesized images with additive noise.

The results show that the DC model optical flow (e) gave many expanded flow fields but no vortex. Note that all flow vectors are presented with different intervals and lengths due to the nonlinear magnitude of each model. The WS model (f) estimated the most uniform flow among all models. The optical flow of the SIN model (g) shows an underestimated flow with a very rough flow. Our model (h) estimated two distinct vortexes with a laminar flow: M = 6, γ =1.6, subblock size =15x15.

Next, in order to verify the robustness of each model, we added Gaussian noise to (a) and (b). The average angular error [11] between the ground truth and four estimated results was quantified. The results of analysis are summarized in Figure 5, where the horizontal and vertical axes represent the standard deviation of additive noise from 3 to 18 per 3 and the angular error, respectively. Noise 0 corresponds to the results of Figure 4 (e - h). The WS model shows the worst result among four models. Our method (M = 6, γ =2.0, subblock size =15x15) was the best, achieving a 50% improvement over the SIN model.

5. Experiment on Real Images

Four real wavy image sequences of a hurricane, smoke, a weak wave, and a strong wave were used to compare optical flow among the three previous methods and our method: *see the supplementary material*.

Hurricane: Figure 6 shows the results of optical flow for the hurricane (a) at time *t* and a flow sketch (b) at time *t+1*. The DC model (c) overestimated the flow and so did the WC model (d). The location of the vortex was not clearly detected. The SIN model (e) only estimated laminar flow in the left upper region with no vortex. Our model (f) (M = 6, γ =2.0, subblock size =20x20) succeeded in estimating a large vortex and discontinuous flow (*see in the dotted ellipse*) around it.
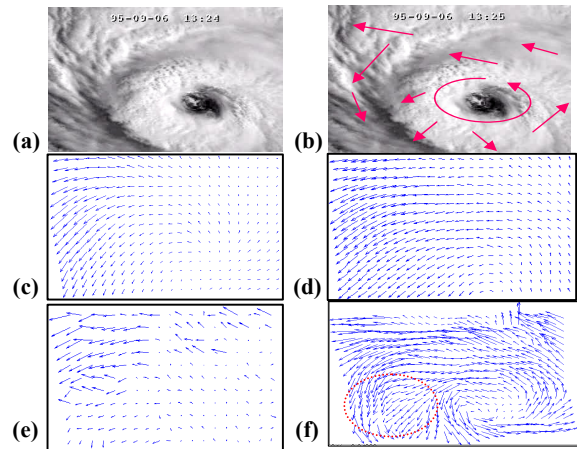

Figure. 6. Comparison of optical flow methods for a hurricane image sequence: 192x128 pixels: (a) Original image. (b) Flow sketch. (c) DC model. (d) WS model. (e) SIN model. (f) Our MI model.

Smoke: Using Figures 7(a) and (b), four results (c-f) of optical flow are shown. The DC model (c) and the SIN model (e) gave similar flows. An expanding and contracting flow appears in the DC model (c). The WS model (d) only detected a translated flow. In the SIN model (e), an underestimated flow was detected everywhere with a strong rightward flow. Our model (f) (M = 3, γ =1.2,

CVPR
#1292

CVPR 2008 Submission 1292. CONFIDENTIAL REVIEW COPY. DO NOT DISTRIBUTE.

CVPR
#1292

subblock size =10x10) estimated a strong upward flow at the bottom of the image and its expansion at the top with a discontinuous flow: *see in the dotted ellipse.*
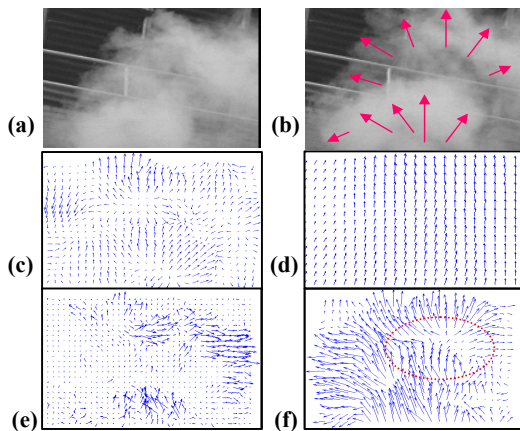

Figure. 7. Comparison of optical flow methods applied to a smoke image sequence: 172x120 pixels: (a) Original image*. (b) Flow sketch. (c) DC model. (d) WS model. (e) SIN model. (f) Our MI model. * *by courtesy of MIT.*
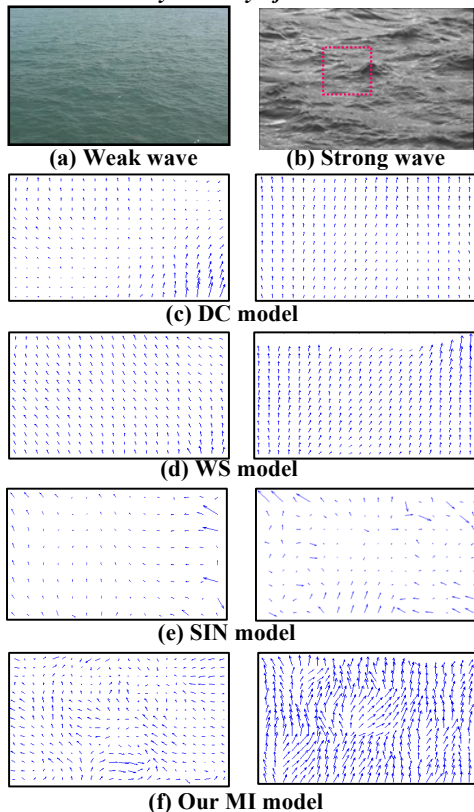

Figure 8: Comparison of optical flow methods for weak and strong* real wave image sequences: 172x115 pixels: * *by courtesy of MIT.*

Wave: Two different wave activities, i.e., weak and strong, in a video were used as shown in Figures 8(a), (b). The results show that two previous methods of the DC (c) and the WS (d) models estimated oversmoothed flows. On the

other hand, (e) estimated a wavy flow from a strong wave only underestimated smooth flow from a weak wave. Thus, in all previous methods, roughness or discontinuous displacements in waves can not be estimated well and no details of the complexity of the wave surface can be found. On the other hand, our MI model (f) estimated a complicated flow that corresponds to the changes in the wave. In particular, a discontinuity in flow was well estimated due to inhomogeneous image intensity and motion. In the second optimization, the Bredtschneider energy spectrum was used via Figures (8) and (9). When the order M = 3~8 was changed for the strong wave image (Fig. 8(b)), the profile estimated frequency distribution was as shown in Figure 10(b). The most similar profile (Fig. 10(b)) comparing with Figure 10(a) was selected. In our model, M = 3/8, γ =1.0/2.0, and subblock size =5x5/20x20 (weak wave/strong wave) were estimated, respectively..
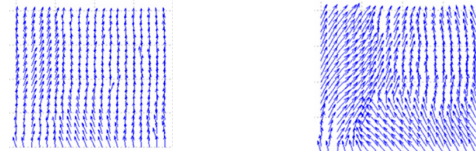
(a) No velocity constraint   **(b) Velocity constraint (γ=2.0)**
Figure 9: Effectiveness of the velocity constraint: magnified view of the red rectangle in Figure. 8(b).

6. Discussion

(Evaluation of optical flow) From Figures 4~8, we conclude that our method was more effective than previous methods. We will discuss the differences among Figures 4-8 as follows: Of the results for the DC and WS models, uniform and smoothed optical flows were commonly estimated for the hurricane (Figs. 6(c), (d)) and wave images (Figs. 8(c), (d)). The flow difference between these two methods can be found in Figures 4(e), (f) and Figures 7(c), (d). In both methods, a local salient flow such as a vortex was either weakly detected or not detected. In the result of smoke (Fig. 7), a more expanding flow in the DC model (c) was detected than in the WS model (d). This suggests that a continuity equation can not locally capture a nonlinear flow. A div-curl velocity constraint played a role mainly in the effects of expansion [7] but the other important flow compared with (f) was detected less. Thus, two of the previous fluid-based models failed to capture not only a wave activity but also dynamic image intensity over time. On the other hand, in Figures. 4(g) and 7(e), the SIN model estimated a more local change in an image than the DC model and WS models. The SIN model estimated a clearer vortex in Figure 4(g) than in Figure 6(e), which can be explained by fact that the image intensity of the hurricane image changed more than that of the synthetic image. This is also comparable to the image intensity change of the smoke (Fig. 7(e)) where a large region of

CVPR
#1292

CVPR 2008 Submission 1292. CONFIDENTIAL REVIEW COPY. DO NOT DISTRIBUTE.

CVPR
#1292

weak flow is estimated in the smoke image. In the wave image (Fig. 8), three models, DC, WC, and SIN gave nearly the same results, which all failed to detect a discontinuous change due to troughs and crests of the wave phenomenon. In our MI method, all flows were estimated as a visually plausible change of a vortex, trough, and crest. The difference between our model (2) and the SIN model (B.2) arises from two properties of the wave generation equation. The first one is that the SIN model does not include a wave orientation parameter. This means that the SIN model is for a single orientation flow but our model is more effective for a multiple orientation flow. The second one is that our model (2) can include a higher spatial frequency as in Figure 8(f) while the SIN model does not mathematically include this. This related to how a discontinuity appears in the estimated flow. Another factor of this discontinuity was due to the velocity constraint (7), the value of γ. For our model, Figure 9 shows the difference between $\gamma = 0$ and $\gamma = 2.0$. This image corresponds to the red boxed region in Figure 8(b). Note that, in the SIN model, no discontinuity was verified for any value of γ even when the setting was done manually, which shows a limitation of the SIN model. For a discontinuous flow detection, Black et al. [12] has shown discontinuous flow detection in a rigid object with a static background; our model however, estimated discontinuous flows in fluid-like image sequences as seen in Figures 6(f), 7(f), and 8(f). These results can not be obtained without the effectiveness of a robust function as in [12]. The MI model with a novel velocity constraint was more important than the use of the robust function.
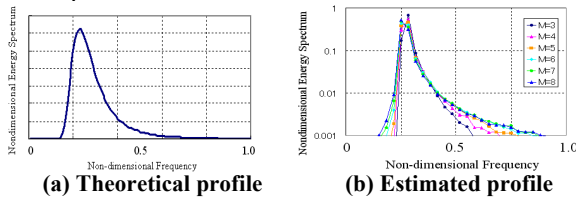

(a) Theoretical profile   (b) Estimated profile

Figure 10: (a) The Bretschneider energy spectrum profile and (b) Estimated profiles of a strong wave for M = 3~8 estimated by our method.
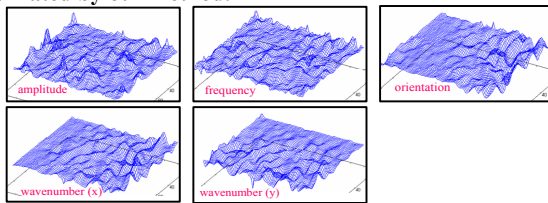

Figure 11: Five wave-related properties estimated by our method for a strong wave (Fig. 8(b)).

(Evaluation of the other properties) In all experiments, our model estimated five wave-related physical properties. However, due to space limitations, we have shown only the results for Figure 8(b) in Figure 11. A quantitative evaluation for these is more difficult than for optical flow

since their units are divided by a frame, i.e., [Hz/frame] in frequency, and the height scales in the five plots are very small. We performed the visual analysis using a video and these five plots. The height variation in Figure 8(b) was similar to an amplitude plot in Figure. 11. A higher frequency was detected overall which corresponds to a strong wave property and both the orientation and the two wavenumber components show a stronger region in the right half than in the left half. Although the SIN model also estimated wave-related parameters, each showed a uniform and nearly flat plot like optical flow. Thus, our MI model was validated for a fluid-like image sequence where inhomogeneous changes in image intensity occurs.
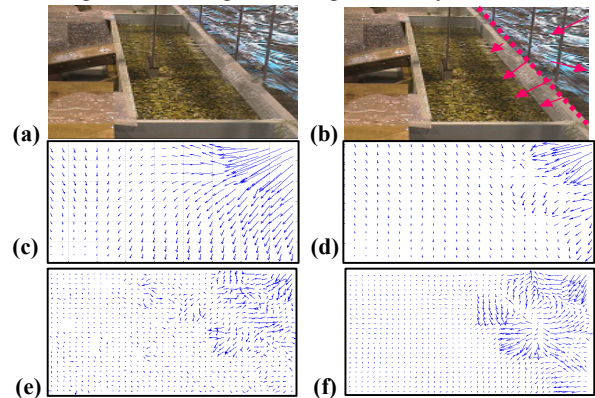

Figure 12: Comparison of optical flow for a real wave image sequence with known motion: 180x120 pixels: (a) Original image*. (b) Flow sketch. (c) DC model. (d) WS model. (e) SIN model. (f) Our MI model. * *by courtesy of Independent Administrative Institution, Port and Airport Research Institute, Japan*

(Additional experiment) We performed an additional wave experiment and limited the verification to one physical property, i.e., orientation. Note that the magnitude of a wave velocity was not used for evaluation. As shown in Figure 12, a one-directional regular wave pattern was mechanically generated in a pool (a). Although the wave was not generated by wind force, the nature of the viscous and the inertial force influenced the wave activities similar to ocean/river waves. A wave train approached the wall of a line (b) and then overflowed like the arrows in the sketch. Part of the wave crossed the wall perpendicular to the line (b) and a reflection wave moved in the opposite direction. We used these wave orientations as the ground truth for evaluating optical flow. The results showed that two previous methods (c) and (d) estimated a smooth flow in the upper right region with no reflecting wave. The SIN model (e) showed similar results to those of our model (f), but the overflowing and reflecting flows moved differently from the ground truth. These results can be a strong smooth constraint to the estimated flow. Among all methods tested, our method (f) gave the most visually plausible flows with M = 6, γ =1.6, and subblock size =15x15. Using an

CVPR
#1292

CVPR 2008 Submission 1292. CONFIDENTIAL REVIEW COPY. DO NOT DISTRIBUTE.

CVPR
#1292

infrared image sequence could remove the uncertainty of the temparature of the water surface. However, such a system is expensive to use and produces blurred images. In all results, three parameters such as M have been estimated so that each parameter becomes large (small) when inhomogenity in an image shows large (small).

7. Conclusion

This paper presents a wave-physical-property-based optical flow method in a fluid-like image sequence where both a smooth and discontinuous flow exist. A novel velocity constraint and the statistical property of waves are also used. Our method surpasses three previous fluid-based models. In future, we will enhance it by modeling changes in the shadows and illumination on the water surface.

References

[1] E. Memin and P. Perez, "Fluid motion recovery by coupling dense and parametric vector fields", IEEE CVPR, pp. 620-625, 1999.

[2] T. Corpetti, E. Memin, and P. Perez, "Dense estimation of fluid flows", IEEE Trans. PAMI, vol. 24, no. 3, pp. 1110-1121, 2002.

[3] R.P. Wildes, M.J. Amabile, A.M. Lanzillotto, and T. S. Leu, "Recovering estimates of fluid flow from image sequence data", CVIU, vol. 80, pp. 246-266, 2000.

[4] Y. Nakajima, H. Inomata, H. Nogawa, Y.Sato, S. Tamura, K. Okazaki, and S. Torii, "Physics-based flow estimation of fluids", Pattern Recognition, vol. 36, pp. 1203-1212, 2003.

[5] L. Zhou, C. Kambhamettu, and D.B. Goldof, "Fluid structure and motion analysis from multi-spectrum 2D cloud image sequence", IEEE CVPR, pp. 744-751, 2000.

[6] D. Bereziat, I. Herlin, and L. Younes, "A generalized optical flow constraint and its physical interpretation", IEEE CVPR, pp. 487-492, 2000.

[7] E. Arnaud, E. Memin, R. Sosa, and G. Artana, "A fluid motion estimator for Schlieren image velocimetry", ECCV, LNCS 3951, pp. 198-210, 2006.

[8] H. Murase, "Surface shape reconstruction of a nonrigid transparent object using refraction and motion", IEEE Trans. PAMI, vol. 14, no. 10, pp. 1045-1052, 1992.

[9] S. Negahdaripour, "Revised definition of optical flow: integration of radiometric and geometric clues for dynamic scene analysis", IEEE Trans. PAMI, vol. 20, no. 9, pp. 961-979, 1998.

[10] H.W. Haussecker and D. J. Fleet, "Computing optical flow with physical models of brightness variation", IEEE Trans. PAMI, vol. 23, no. 6, pp. 661-673.

[11] J.L. Barron, D.J. Fleet, and S.S. Beauchemin, "Systems and experimental performance of optical flow techniques", Int'l J. Computer Vision, vol. 12, pp. 43-77, 1994.

[12] M.J. Black and P. Anandan, "The robust estimation of multiple motions: parametric and piecewise-smooth flow fields", CVIU, vol. 63, no. 1, pp. 75-104, 1996.

[13] B. Jahne and S. Wass, "Optical wave measurement technique for small scale water surface waves", Proc. Advances in Optical Instruments for Remote Sensing, pp. 147-152, 1989.

[14] T.K. Holland, "Application of the linear dispersion relation with respect to depth inversion and remotely sensed imagery", IEEE Trans. GRS, vol. 39, no. 9, pp. 2060-2072, 2001.

[15] L. Spencer, M. Shah, and R.K. Guha, "Determining scale and sea state from water video", IEEE Trans. IP, vol. 15, no. 6, pp. 1525-1535, 2006.

[16] M. Sun, A.D. Jepson, and E. Fiume, "Video input driven animation (VIDA)", IEEE Int. Conf. Computer Vision, pp. 96- 103 vol.1, 2003.

[17] J. Tessendorf, "Simulating ocean water", SIGGRAPH, in Course Notes, 1999.

[18] B. Kinsman, "Wind waves: their generation and propagation on the ocean surface", Prentice-Hall, 1965.

[19] K. Horikawa, "An introduction to ocean engineering",Tokyo Univ. Press, 2004.

[20] K. Otsuka, T. Horikoshi, and S. Suzuki, "Image velocity estimation from trajectory surface in spatiotemporal space", IEEE CVPR, pp. 200-205, 1997.

[21] H. Sakaino, "The PhotoDynamic Tool: generation of animation from a single texture image", IEEE Int'l Conf. Multimedia and Expo, 2005.

[22] G. Doretto and S. Soatto, "Editable dynamic textures", IEEE CVPR, pp. 137-142, 2003.

Appendix A

To begin with, a dispersion relationship between the velocity and frequency is used to derive the novel velocity constraint in this paper.

$$c = \frac{\omega}{k} = \sqrt{\frac{g}{k}\tanh(kh)} \therefore c = \frac{g}{2\pi f}\tanh\left(\frac{2\pi f}{c}h\right) \quad (A.1)$$

where c is a velocity (optical flow). A Taylor expansion series of $\tanh(x)$ shows the following.

$$\tanh(x) = x - \frac{1}{3}x^3 + \frac{2}{15}x^5 - \frac{17}{315}x^7 + \cdots.$$

Using this, (A.1) becomes

$$c = \frac{g}{2\pi f}\left(\frac{2\pi f}{c}h - \frac{1}{3}\left(\frac{2\pi f}{c}h\right)^3\right) \text{ where } \left|\frac{2\pi f}{c}h\right| < \frac{\pi}{2} \therefore \left|\frac{fh}{c}\right| < \frac{1}{4}. \quad (A.2)$$

With respect to velocity c, this can be transformed as follows:

$$c^4 - ghc^2 + \frac{4}{3}\pi^2 gh^3 f^2 = 0 \quad \therefore c^2 = gh \pm \sqrt{(gh)^2 - \frac{16}{3}\pi^2 gh^3 f^2}/2 \quad (A.3)$$

For a real solution, c^2 must satisfy the following condition:

$$(gh)^2 \ge \frac{16}{3}\pi^2 gh^3 f^2 \qquad \therefore f^2 \le \frac{3g}{16\pi^2 h} \quad (A.4)$$

When we select a positive solution, the relationship between a frequency f and velocity c is given by

$$c^2 \propto \sqrt{(gh)^2 - \frac{16}{3}\pi^2 gh^3 f^2} \Rightarrow \therefore c \propto \left(3g/(16\pi^2 hf^2)\right)^{1/4} $$

Finally, we obtain a new velocity constraint for wave motion.

$$c^2 \propto |\gamma - f^2|^{1/2}. \text{ where } \gamma = \frac{3g}{16\pi^2 h}. \quad (A.5)$$

Appendix B

Here, we give a brief description of two of the previous methods. First, a fluid-based optical flow model applies a continuity equation and a div-curl velocity constraint [2] as shown in (B.1).

$$E = \iint_\Omega \left(\frac{\partial I}{\partial t} + \mathbf{u}\cdot div(I)\right) d\Omega + \iint_\Omega (\lambda_3^2 div^2 \mathbf{u} + \lambda_4^2 curl^2 \mathbf{u}) d\Omega$$

$$= \iint_\Omega \left(I\frac{\partial u}{\partial x} + I\frac{\partial v}{\partial y} + I_x u + I_y v + I_t\right)^2 d\Omega + \iint_\Omega \{\lambda_3^2\left(\frac{\partial u}{\partial x} + \frac{\partial v}{\partial y}\right)^2 + \lambda_4^2\left(\frac{\partial v}{\partial x} - \frac{\partial u}{\partial y}\right)^2\} d\Omega$$

$$(B.1)$$

where two empirically determined control parameters are $\lambda_3 = 10^6$, $\lambda_4 = 10^{-6}$. The first term on the right hand side of (B.1) is used in [3] with a smooth velocity constraint. Second, the simplest wave equation (B.2) is used from [8]. Here, we have amplitude a_q, order Q, wavenumber (k_q^x, k_q^y), and image intensity $H_{\sin}(x, y, t)$. We apply (B.3) to (4) with no velocity constraints.

$$H_{\sin}(x,y,t) = \sum_{q=1}^{Q} a_q \sin(xk_q^x + yk_q^y - 2\pi f_q t). \quad (B.2)$$

$$\frac{d(physics)}{dt} \equiv \frac{dH_{\sin}(x,y,t)}{dt}. \quad (B.3)$$